Fourier transform spectroscopy and extended deperturbation treatment of the spin-orbit-coupled $A\,^1\Sigma_u^+$ and $b\,^3\Pi_u$ states of the Rb_2 molecule

A. N. Drozdova,[1,3] A. V. Stolyarov,[1] M. Tamanis,[2] R. Ferber,[2] P. Crozet,[3] and A. J. Ross[3,*]

[1]*Department of Chemistry, Lomonosov Moscow State University, GSP-1 Leninskie gory 1/3, Moscow 119991, Russia*

[2]*Laser Center, University of Latvia, Rainis Boulevard 19, LV-1586 Riga, Latvia*

[3]*Institut Lumière Matière, UMR 5306 Université Lyon 1 - CNRS, Université de Lyon, 69622 Villeurbanne, France*

(Received 5 June 2013; published 9 August 2013)

Fourier transform records of $A\,^1\Sigma_u^+ - b\,^3\Pi_u \rightarrow X\,^1\Sigma_g^+$ and $(2)\,^1\Pi_g \rightarrow A\,^1\Sigma_u^+ - b\,^3\Pi_u$ laser-induced fluorescence in hot rubidium vapor have identified more than 4500 rovibronic term values in the spin-orbit-coupled $A\,^1\Sigma_u^+$ and $b\,^3\Pi_u$ states of Rb_2. We report a 4×4 coupled-channel deperturbation analysis of some 6100 term energies in $^{85}Rb_2$ and $^{85}Rb\,^{87}Rb$, including term values taken from papers by Salami *et al.* [Phys. Rev. A **80**, 022515 (2009)], Amiot *et al.* [Phys. Rev. Lett. **83**, 2316 (1999)], and Amiot [J. Chem. Phys. **93**, 8591 (1990)]. Spin-orbit and spin-rotation interactions between $A\,^1\Sigma_u^+$ and $b\,^3\Pi_{u(\Omega=0,1,2)}$ are taken into account explicitly, fitting to analytical potential curves of the interacting $A\,^1\Sigma_u^+$ and $b\,^3\Pi_{0u}$ states and to r-dependent diagonal and off-diagonal spin-orbit-coupling functions. The resulting mass-invariant fitting parameters reproduce 96% of all available experimental term values of the $A - b$ complex for all Rb_2 isotopologs (covering 93% of the $A\,^1\Sigma_u^+$ potential energy well) with a standard deviation of 0.005 cm^{-1}, matching experimental uncertainties estimated to be $\leqslant 0.01$ cm^{-1}.

DOI: 10.1103/PhysRevA.88.022504 PACS number(s): 31.50.Df, 31.15.aj

I. INTRODUCTION

The strong spin-orbit interactions between the deeply bound $A\,^1\Sigma_u^+$ and $b\,^3\Pi_u$ states of the heavier alkali-metal dimers have long been a subject of interest (and sometimes of annoyance) to spectroscopists. They produce complicated patterns in optical spectra and offer a longstanding challenge as to how to represent this set of energy levels. Double-resonance excitation experiments have exploited strongly mixed levels to access the triplet-state manifold, starting from thermally populated levels of the electronic ground state, in what became known as the "PFOODR" technique (perturbation-facilitated optical-optical double resonance [1]). Enhanced access to the triplet manifold has sometimes been achieved with specific collisional processes, too, via the "gateway" effect [2]. Recent work in the context of cold molecules taps into these levels from the opposite direction, because the coupled levels are useful intermediates on the (spin-forbidden) optical route back to vibrationally cold ground-state molecules, when starting from the vibrationally hot triplet species typically formed by photoassociation of cold atoms. Because the $A\,^1\Sigma_u^+$ and $b\,^3\Pi_u$ states are deeply bound "short-range" molecular states, they are a poor choice for optical transfer to very low vibrational levels in a single-step process. But accurate descriptions of a wide range of these intermediate states become more pertinent as increasingly complex optical routes, involving several photons, are (according to recent experiments [3] and review [4]) considered and employed to transfer ultracold molecule populations to the lowest singlet vibrational level. This work aims to describe the short-range part of the $A\,^1\Sigma_u^+$ state of Rb_2 and its interactions with the $b\,^3\Pi_u$ state, and to predict possible singlet-triplet transfer regions for rotationally cold rubidium dimers.

Single-state models for the $A\,^1\Sigma_u^+$ and $b\,^3\Pi_{0u}$ states of the rubidium dimer are inappropriate; the energy-level shifts induced by spin-orbit effects make it sometimes difficult even to recognize vibrational patterns [5]. Effective Hamiltonians have been used to describe restricted numbers of interacting levels of these two states in lighter dimers (see, for example, Ref. [6]) but have the drawbacks of requiring large numbers of correlated parameters, and of being unsuited to any kind of extrapolation. The coupled-channel (CC) deperturbation approach, developed notably by Stolyarov *et al.* [7] and by Bergeman [8,9] for the $A - b$ complexes in alkali dimers, has overcome this by using appropriate analytical forms to represent two interacting diabatic states, with radially variant matrix elements between them taken either as pointwise *ab initio* functions, or as a chosen empirical analytical function. The potential forms can be forced to accommodate some physical constraints, for example, dissociation energies, long-range behavior, or known equilibrium distances, with a modest number of fitting parameters, in an extension of the single-state treatment promulgated by, among others, Le Roy [10]. The CC deperturbation method has been successfully applied even to the most heavily coupled Rb- and Cs-containing species: Rb_2 [11], Cs_2 [12], NaRb [7,13], RbCs [9,14], NaCs [15], and KCs [16,17]. To achieve reliable results, these fits still require an extensive and representative data set from which the potential energy functions and diagonal and off-diagonal spin-orbit functions are optimized. This work builds on experimental foundations laid in the 1990s in Orsay at Laboratoire Aimé Cotton (LAC), with Fourier-transform (FT)-resolved laser-induced fluorescence (LIF) by single- [10,18] or double-resonance [5] excitation, and extends the numerical treatment performed by Salami *et al.* [11] with a smaller data set of energy levels lying below 14 000 cm^{-1}.

We have performed two series of resolved fluorescence experiments, shown schematically in Fig. 1, aiming to bridge

*amanda.ross@univ-lyon1.fr

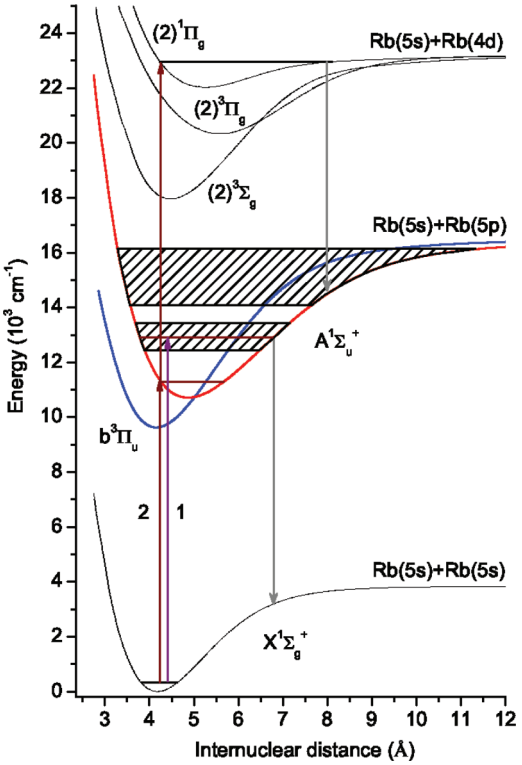

FIG. 1. (Color online) Laser excitation pathways and fluorescence detected by Fourier transform spectrometry, used to explore uninvestigated regions (shaded areas) of the $A - b$ complex: (1) direct excitation of rovibronic levels and (2) one- and two-color double-resonance excitation.

the gap between the assigned levels treated in Ref. [11] and the series observed but unassigned in earlier double-resonance work [5]. $A \rightarrow X$ fluorescence has been recorded in Lyon and in Riga, (i) covering a modest set of vibronic levels in the range 12 000–13 000 cm^{-1}, with rotational relaxation increasing the spread of rotational levels in some cases, and (ii) giving almost complete coverage of the lowest vibrational levels of the $A\,^1\Sigma_u^+$ state, below 11 000 cm^{-1}. We also undertook a set of one- or two-color double-resonance experiments, pumping the $(2)\,^1\Pi_g$ state, and recording FT-resolved fluorescence spectra to probe higher levels of the $A\,^1\Sigma_u^+$ state than can be readily accessed in single-photon absorption from the ground state. The aim was to overlap observations from the two sets of experiments, and to cover as much of the $A\,^1\Sigma_u^+ - b\,^3\Pi_u$ complex as possible. The $\Omega = 0_u^+$ component of $b\,^3\Pi_u$ is observed through a multitude of perturbations with $A\,^1\Sigma_u^+$. Only a small fraction of the observed levels have significant $\Omega = 1$ or $\Omega = 2$ character. Several attempts were made to observe the $b\,^3\Pi_u$ state directly, from some higher-lying triplet state, but none has so far been successful. Work at Temple University [19] did indeed access a single $^3\Lambda_g$ level at $J' = 69$ by PFOODR. Strong fluorescence was observed to the lowest triplet state of Rb_2 ($a\,^3\Sigma_u^+$), but we found no evidence of emission to the higher-lying $b\,^3\Pi_u$ state when we tried to pump the same upper state, possibly because it was swamped by the stronger $A \rightarrow X$ emission.

We outline the experimental contribution in Sec. II of the paper. Section III describes the final set of term energies ($^{85}Rb_2$ and $^{85}Rb\ ^{87}Rb$) that have been taken as input material for the deperturbation treatment presented in some detail in Sec. IV. We also discuss the question of assignments and calibration in this section: comparison of term values for identical energy levels derived from different spectra or sources revealed some systematic differences which are detrimental to the final data reduction process. The empirical potential energy curves and spin-orbit functions resulting from the deperturbation fit are given in Sec. V, giving comparisons with recent *ab initio* calculations. The last section illustrates some "quality control" tests. We have used the results from the fit of data for the two main isotopologs to predict energies for some levels of $^{87}Rb_2$, and compare them with experimentally determined energies. We also compare the measured and calculated intensity distributions for $A - b \rightarrow X$ LIF series coming from heavily mixed levels ($v_A = 0$ and 39) of the $A - b$ complex, assuming that the transition dipole moment for the spin-forbidden $b\,^3\Pi_u - X\,^1\Sigma_g^+$ transition is zero.

II. EXPERIMENT

The excited $A\,^1\Sigma_u^+$ and $b\,^3\Pi_u$ states in Rb_2 have been the main focus of three high-resolution spectroscopic studies [5,11,20]. A compilation of all available experimental term values of the $A\,^1\Sigma_u^+ - b\,^3\Pi_u$ complex revealed areas where the data became rather sparse (12 000–13 000 cm^{-1}, and above 14 000 cm^{-1}), so that the parameters given in Ref. [11] could not be extrapolated far enough to give vibrational assignments for the $(2)\,^1\Pi_g \rightarrow A\,^1\Sigma_u^+ - b\,^3\Pi_u$ fluorescence transitions observed in Orsay (LAC) [5], although their rotational numbering and parity assignments were secure.

Resolved fluorescence spectra, recorded on Fourier transform instruments following single- or double-resonance excitation, provide information on the $A\,^1\Sigma_u^+ - b\,^3\Pi_u$ complex, in particular, for the shaded areas indicated in Fig. 1. Franck-Condon windows allow the lower part of the $A\,^1\Sigma_u^+$ potential curve to be accessed directly from the ground state. Well-resolved $A \rightarrow X$ fluorescence spectra were recorded and analyzed. Energies of levels in the electronic ground state are accurately established [10], so measured transitions in a selection of bands can provide upper-state energies directly, with uncertainties reflecting spectral resolution, absolute calibration, and Doppler widths for the transitions used. The higher part of the $A\,^1\Sigma_u^+$ state region was explored by means of the optical-optical double-resonance (OODR) excitation described in Ref. [5], detecting $(2)\,^1\Pi_g \rightarrow A\,^1\Sigma_u^+ - b\,^3\Pi_u$ fluorescence in the region 6000–11 000 cm^{-1}, with added flexibility of two-color double-resonance excitation. Converting measured wave numbers for the $(2)\,^1\Pi_g \rightarrow A\,^1\Sigma_u^+ - b\,^3\Pi_u$ transitions to term energies for the $A\,^1\Sigma_u^+ - b\,^3\Pi_u$ complex was less straightforward. Strong atomic transitions Rb($4d$)→Rb($5p$) and Rb($6s$)→Rb($5p$) ensured reliable calibration for transition wave numbers, but these transitions are not directly connected to the molecular energy reference, i.e., the minimum of the electronic ground state. We have taken the $B\,^1\Pi_u$ state as a secondary energy reference, analyzing $(2)\,^1\Pi_g \rightarrow B\,^1\Pi_u$ transitions as well as the $(2)\,^1\Pi_g \rightarrow A\,^1\Sigma_u^+ - b\,^3\Pi_u$ system of primary interest, since the upper state is common to both, and the low levels of the $B\,^1\Pi_u$ state are almost unperturbed.

In all the experiments, rubidium vapor was produced in heat-pipe sources using higher-than-usual buffer gas pressures (around 9 mbar argon, with heat-pipe temperatures ~300°C) to enhance rotational energy transfer in the excited states. The heat pipe used in Riga was in fact designed to produce RbCs; the experiment is described in detail elsewhere [14]. Rb_2 vapor was excited around 980 nm with ~30 mW emission from a single-mode diode laser (L980P200I from Thorlabs). Fluorescence was detected on a room-temperature InGaAs detector using the preview mode of the Bruker IFS 125HR instrument to discriminate between fluorescence from rubidium dimer and fluorescence from RbCs. Rb_2 signals dominate with laser wave numbers of 10 150–10 360 cm^{-1}, corresponding to excitation of very low vibrational levels of the $A\,^1\Sigma_u^+$ state from vibrationally excited levels of the ground state. The spectra in Riga were recorded at an instrumental resolution of 0.03 cm^{-1}; we estimate uncertainties in the associated term energies of 0.01 cm^{-1}, originating mostly from Doppler broadening. The FT instruments used to record the spectra typically allow well-separated peaks with S/N ratios greater than 3 to be determined (and reproduced) to 1/10 of the effective resolution, which is a convolution of instrumental line shape and Doppler profiles in these experiments. Absolute line position uncertainties are more difficult to assess, since it is not always possible to assert that transitions are pumped at the line center. Systematic shifts can then occur within the Doppler profile. At 10 000 cm^{-1}, at typical heat-pipe temperatures, the Doppler width (FWHM) is about 0.013 cm^{-1} for Rb_2.

$A\,^1\Sigma_u^+ - b\,^3\Pi_u \rightarrow X\,^1\Sigma_g^+$ fluorescence in the Riga experiment was characterized by rich rotational relaxation, sometimes populating dominantly triplet character levels, demonstrating the vibronic "gateway" effect (collisional populations enhanced by perturbation), first evoked by Gelbart and Freed [21]. This is illustrated in Fig. 2. The laser pumps $J_{A-b} = 150$ in the lowest $v_A = 0$ level of the $A\,^1\Sigma_u^+$ state via R(149) 0–9 $A \leftarrow X$. Collisional energy transfer

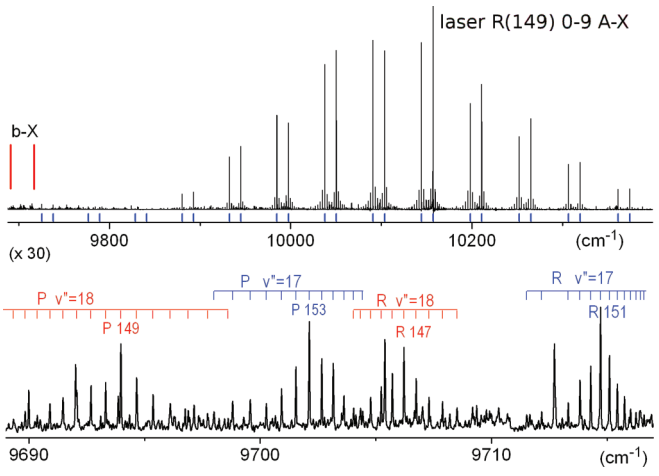

FIG. 2. (Color online) Direct laser-induced fluorescence excited via $R(149)\ 0-9\ A \leftarrow X$ ($\nu_{laser} = 10\,157.18\ cm^{-1}$) showing in the upper part strong $A \rightarrow X$ doublets, with rotational relaxation satellites (ΔJ_{A-b} even). The lower trace enlarges the section indicated by vertical bars (vertical scale ×30). It shows collisionally induced fluorescence from two vibrational levels of $b\,^3\Pi_{0u}$ whose rotational levels 140–160 have >30% $A\,^1\Sigma_u^+$ character.

populates levels $J_{A-b}^{even} = 138$–166 in this state, but also in the two strongly interacting vibrational levels of $b\,^3\Pi_{0u}$ lying immediately above and below $v_A = 0$ of the A state. The transitions from the dominantly $b\,^3\Pi_{0u}$ levels become easier to recognize once Franck-Condon overlap becomes small for the "spin-allowed" $A \rightarrow X$ fluorescence depicted in the upper section of Fig. 2. The lower part of Fig. 2 illustrates a very small part of the left-hand side of the upper trace, showing formally "spin-forbidden" $b\,^3\Pi_u \rightarrow X\,^1\Sigma_g^+$ transitions from these two $b\,^3\Pi_{0u}$ levels. The strongest lines in the higher-energy bands (transitions from the $b\,^3\Pi_{0u}$ level below $v_A = 0$ of $A\,^1\Sigma_u^+$ to $v_X'' = 17$ in $X\,^1\Sigma_g^+$) come from $J_{A-b} = 152$; the strongest lines in the other bands (with the lower set of markers) peak at $J_{A-b} = 148$. The intensities reflect not only the initial value of J_{A-b}, but also highlight rotational levels having more than 30% $A\,^1\Sigma_u^+$ character.

In Lyon, $A\,^1\Sigma_u^+ \rightarrow X\,^1\Sigma_g^+$ fluorescence was excited initially with a ring dye laser (SP 380D) operating with Styryl 9 dye (826–866 nm) and later with emission from a CR-899 Ti:sapphire laser with midrange optics (765–855 nm). Single-mode output powers were typically 40 and 300 mW, respectively. These shorter wavelengths excite in a region of higher density of states, where fluorescence lifetimes are shorter. This results in more complicated spectra, as several weaker series are excited simultaneously, with fewer rotational satellites (see Fig. 3). About 40 such spectra were recorded (InGaAs or Si-avalanche detector, on a Bomem DA3 instrument), at resolutions from 0.03 to 0.08 cm^{-1}. Uncertainties were estimated as a convolution of Doppler width and 1/10 instrumental resolution. The $A \rightarrow X$ transitions from which $A - b$ term energies were deduced are given in the Supplemental Material [22].

Double-resonance experiments (OODR) were also performed in Lyon, initially with a single Ti:sapphire laser, looking for fortuitous single-color double-resonance signals. These were recognized by an increase in the total fluorescence detected through $\lambda > 1.1\ \mu m$ filters. Rotationally resolved spectra were recorded on a liquid-air cooled InGaAs detector, using less severe filters ($\lambda > 1\ \mu m$) to attenuate only the strongest part of the $A - X$ system (see Fig. 4). From the earlier work in Orsay (LAC) [5,23], we expected emission to $A\,^1\Sigma_u^+$ and $B\,^1\Pi_u$ in the 6400–9500 cm^{-1} region accessible in these conditions, when the $(2)\,^1\Pi_g$ was populated. It eventually became clear that many double-resonance signals were heavily dominated by atomic lines (see Fig. 4), and that the majority of molecular transitions were to the $B\,^1\Pi_u$ state, with little or no emission to the $A - b$ complex in the 6400–9500 cm^{-1} window (selected by the onset of detection at the long wavelength side, and $\lambda > 1000$ nm high-pass filters at the other). A narrow range of upper-state energies 23 000–23 200 cm^{-1} provides a window from which fluorescence occurs principally to the $A\,^1\Sigma_u^+ - b\,^3\Pi_u$ complex, with weaker emission to the $B\,^1\Pi_u$ state.

When a second Ti:sapphire laser became available, a more systematic approach to OODR was adopted. Output from a Matisse TS laser (long-wave optics, operating around 900–940 nm) was scanned while the wavelength from the CR-899 laser remained fixed. The lasers were copropagated, and backwards fluorescence was again recorded through $\lambda > 1\ \mu m$ filters. Strong signals were recorded at a resolution

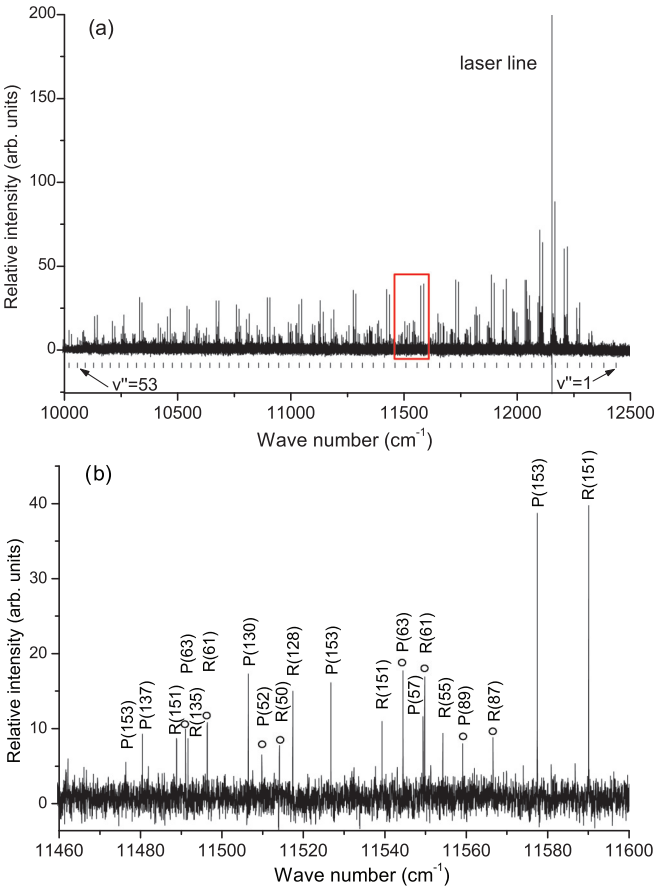

FIG. 3. (Color online) Fluorescence excited by $\nu_{\text{laser}} = 12\,154.58$ cm^{-1} from Styryl 9 dye. (a) Overview of the strongest progression corresponds to $R(151)$, $p(153)$ doublets from $J_{A-b} = 152$ in the $A - b$ complex. (b) Close-up view shows transitions from seven upper-state levels pumped simultaneously by the laser. Open circles ○ indicate transitions in ^{85}Rb ^{87}Rb.

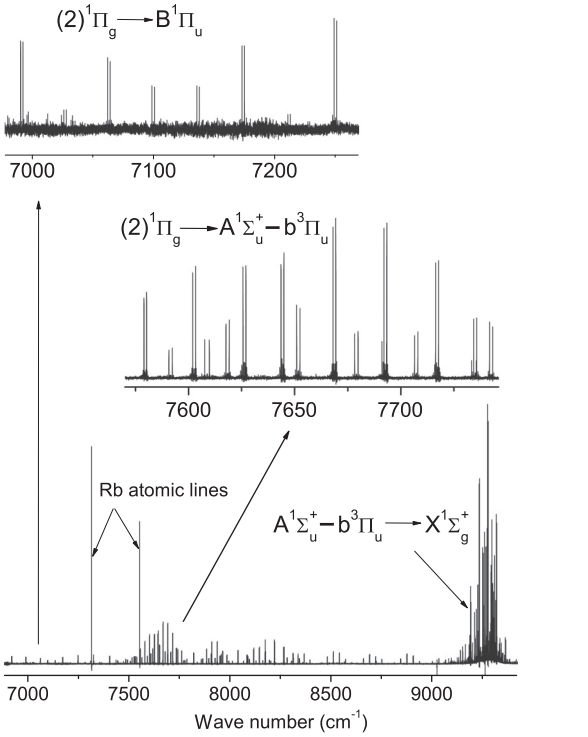

FIG. 4. Fluorescence from $^{85}Rb_2$ following single-color OODR excitation at $\nu_{\text{laser}} = 11\,554.966$ cm^{-1}. Both $(2)\,^1\Pi_g \rightarrow A - b$ and $(2)\,^1\Pi_g \rightarrow B\,^1\Pi_u$ transitions from a common upper level, $J' = 31e$, are observed in this energy region.

of 0.04 cm^{-1} and weaker ones at 0.08 cm^{-1}. We could not predict the upper-state energies accurately when this work was done, and exploratory scans took quite some time. The paper by Han *et al.* [24] describing the $(2)\,^1\Pi_g$ state, published in 2012, has since allowed us to make some vibrational assignments for the upper state of the double-resonance experiment.

III. SPECTRA AND ANALYSIS

Table I summarizes the results from our $(2)\,^1\Pi_g \rightarrow A\,^1\Sigma_u^+ - b\,^3\Pi_u$ Fourier transform spectroscopy (FTS) resolved fluorescence spectra. Isotopic and rotational assignments were made from combination differences in the $B\,^1\Pi_u$ state. Parity assignments in the $(2)\,^1\Pi_g$ state were obvious from the fluorescence to the $A\,^1\Sigma_u^+$ state: either Q or P and R branches were observed. Around 2500 $(2)\,^1\Pi_g \rightarrow A\,^1\Sigma_u^+ - b\,^3\Pi_u$ transition wave numbers have been measured, including collisionally induced rotational relaxation lines. At least 1/3 of the nominally $(2)\,^1\Pi_g \rightarrow A\,^1\Sigma_u^+$ transitions in these LIF series were accompanied by extra lines, giving a good deal of direct information on the 0_u^+ component of the $b\,^3\Pi_u$ state. None of the extra lines in this system had dominant $b\,^3\Pi_{1u}$ or $b\,^3\Pi_{2u}$ character.

The range of the Rb_2 $A - b$ term values used in this work is shown in Fig. 5. A compilation of assigned lines and calculated term values is given in the Supplemental Material [22]. In summary, there were 3391, 2785, and 53 $^{85}Rb_2$, ^{85}Rb ^{87}Rb, and $^{87}Rb_2$ term values, respectively, in the data set, covering the energy range $E_{A-b} \in [10\,801, 16\,400]$ cm^{-1} and rotational quantum numbers $J_{A-b} \in [6, 258]$ (see Table II).

IV. DEPERTURBATION ANALYSIS

We assume that all molecular parameters of the deperturbation model (describing the potential energy curves and spin-orbit functions) are mass independent. Our analysis is based on simultaneous fits to experimental term values of $^{85}Rb_2$ and ^{85}Rb ^{87}Rb isotopologs (representing 98.9% of the data set), indicated in Fig. 5. The remaining data for the $^{87}Rb_2$ molecule were used to test the model: the $^{87}Rb_2$ rovibronic term values have been predicted from the parameters obtained from fitting $^{85}Rb_2$ and ^{85}Rb ^{87}Rb energies and compared with their experimental counterparts.

A. Modeling Hamiltonian

Deperturbation analysis [25] of rovibronic structure in the singlet-triplet $A - b$ complex in Rb_2 was performed using the coupled-channel (CC) technique [7–9,11–17,26,27]. Within the framework of the CC approach, the total nonadiabatic rovibronic wave function Ψ_j^{CC} corresponding to the jth rovibronic level of the $A - b$ complex with the fixed rotational

TABLE I. Laser excitation wave numbers producing $(2)^1\Pi_g \rightarrow A-b$ molecular fluorescence in OODR experiments. Analysis of $(2)^1\Pi_g \rightarrow B^1\Pi_u$ transitions provided rotational assignments and upper-state term values, T'. E_{A-b} indicates the range of rovibronic energies in the $A-b$ complex observed in fluorescence, given by $T' - \nu_{(2)^1\Pi_g \rightarrow A-b}$.

v''_X	J''_X	ν_{laser_1} (cm^{-1})	J_{A-b}	ν_{laser_2} (cm^{-1})	v'	J'	T' (cm^{-1})	E_{A-b} (cm^{-1})
				$^{85}Rb_2$				
0[b]	70	11443.130	69		39	69f	23025.993	14085–14552
0	57	11544.190	58	11393.810	38	57e	23040.649	14255–14650
0	86	11428.755	85		36	86e	23053.084	13990–14550
2	57	11425.792	56		40	57e	23068.695	14000–14900
0	57	11544.190	58	11424.106	40	58f	23069.814	13990–14940
				11398.805	40	59e	23070.944	14190–14910
2	71	11421.415	72		41	72f	23099.949	14120–15145
0	29	11554.966	30		50	29e	23158.373	14095–15755
0	111	11433.922	110		42	110f	23172.859	14020–15380
0[b]	9	11573.748	8		53	7e	23178.367	15265–15800
0[a]	28	11572.876	29		54	30e	23192.879	14065–15930
0	96	11497.965	97		51	98e	23232.074	14200–16310
0[a]	73	11556.685	72			72f	23262.787	14125–16200
1	31	11581.486	32			31e	23271.567	14220–16270
0[b]	81	11558.165	82			82f	23293.211	16045–16300
0	129	11398.807	130	11544.190		130f	23343.330	14370–16403
				$^{85}Rb^{87}Rb$				
0		11430.866	83		36	83f	23043.886	14190–14440
1	70	11427.737	69		38	68e	23050.749	14000–14680
0	55	11501.644	54		43	54f	23100.063	14040–15280
0	46	11539.220	45		49	44e	23154.975	14025–16120
2	95	11424.202	94		47	93e	23189.371	11340–11560
0	81	11543.390	80			79e	23260.839	14120–16630
1	38	11574.105	39			38e	23266.822	15080–16220
1[a]	39	11573.690	40			40f	23267.724	14340–16230
1	40	11573.282	41			42e	23268.645	14980–16220
0	68	11571.308	69	-		69f	23274.895	14165–16480
3	61	11544.190	62	11486.860		62f	23275.044	14275–16250
0	91	11545.490	92	-		91e	23303.851	14310–16615
0[a]	99	11531.560	98	-		97e	23309.575	14220–16550
0	100	11537.233	101	-		101f	23325.301	14360–16410
3	61	11448.684	62	11543.490		61e	23274.390	14275–16255

[a]Series also seen in Ref. [5], re-recorded in this work.
[b]data taken from the $(2)^1\Pi_g \rightarrow A-b$ spectra of Ref. [5].

quantum number J and e parity is approximated by the linear combination of symmetrized electronic-rotational wave functions φ_i belonging to a pure Hund's coupling case "**a**" [25], $\Psi_j^{CC} = \sum_i^M \phi_i \varphi_i$. The subscript i refers to an adiabatic electronic state, and the mixing coefficients ϕ_i are defined by a system of M coupled radial equations:

$$\left(-\mathbf{I}\frac{\hbar^2 d^2}{2\mu dr^2} + \mathbf{V}(r;\mu,J) - \mathbf{I}E_j^{CC}\right)\Phi_j(r) = 0, \qquad (1)$$

with the conventional boundary $\phi_i(0) = \phi_i(\infty) = 0$ and normalization condition $\sum_i^M P_i = 1$, where $P_i = \langle\phi_i|\phi_i\rangle$ is the fraction partition of the jth state. $\mathbf{I}$ is the identity matrix, E_j^{CC} is the total nonadiabatic energy of rovibronic level of the complex, $\mathbf{V}$ is the matrix of potential energy, μ is the reduced molecular mass, and J is the rotational quantum number.

In this study we have adopted the 4×4 modeling Hamiltonian [28] used to describe the equivalent in the $A-b$ complex in KCs [16,17]. The (symmetric) potential energy matrix has the following diagonal

$$\begin{aligned} V_{^1\Sigma^+} &= U_A + B[X+2] \\ V_{^3\Pi_0} &= U_{b0} + B[X+2] \\ V_{^3\Pi_1} &= U_{b0} + A_{01}^{so} + B[X+2] \\ V_{^3\Pi_2} &= U_{b0} + A_{01}^{so} + A_{12}^{so} + B[X-2] \end{aligned} \qquad (2)$$

and nonzero off-diagonal

$$\begin{aligned} V_{^1\Sigma^+-{}^3\Pi_0} &= -\sqrt{2}\xi_{Ab0}^{so} \\ V_{^3\Pi_0-{}^3\Pi_1} &= -B\sqrt{2X} \\ V_{^3\Pi_1-{}^3\Pi_2} &= -B\sqrt{2(X-2)} \\ V_{^1\Sigma^+-{}^3\Pi_1} &= -B\zeta_{Ab1}^{so}\sqrt{2X} \end{aligned} \qquad (3)$$

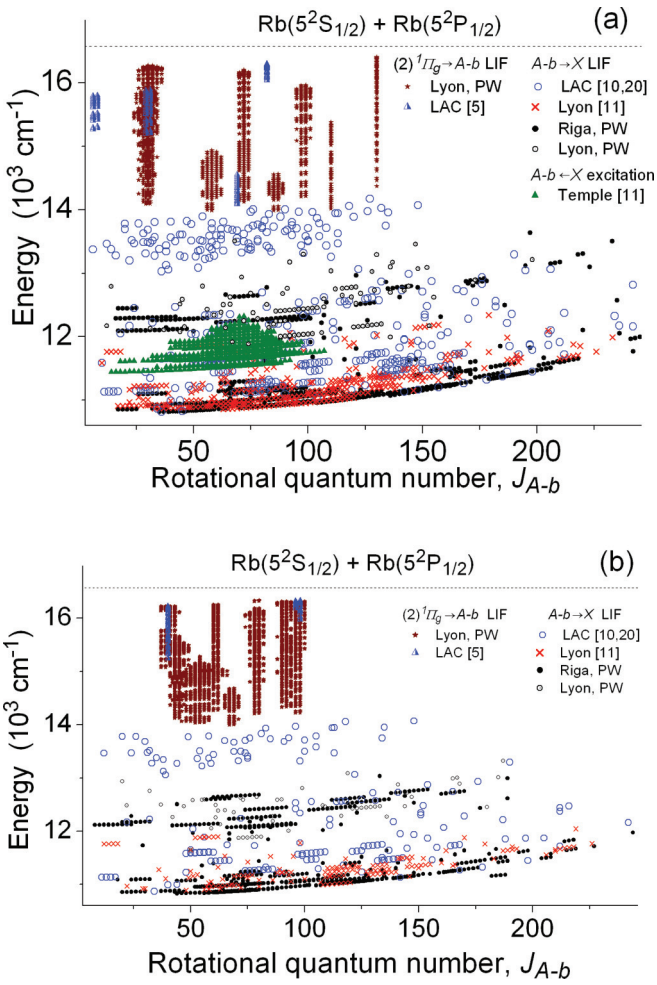

FIG. 5. (Color online) Data set of the Rb_2 $A-b$ complex used for the deperturbation analysis: (a) $^{85}Rb_2$ and (b) $^{85}Rb\,^{87}Rb$.

matrix elements [28], where

$$B \equiv \frac{\hbar^2}{2\mu r^2}; \quad X \equiv J(J+1).$$

The key parameters of this model are the diabatic potential energy curves of the interacting singlet $A\,^1\Sigma_u^+$ and triplet $b\,^3\Pi_{0u}$ states, $U_A(r)$, $U_{b0}(r)$, the spin-orbit-coupling matrix element $\xi^{so}_{Ab0}(r)$, and the nonequidistant spin-orbit splitting functions $A^{so}_{01}(r)$ and $A^{so}_{12}(r)$. An additional empirical r-independent parameter ζ^{so}_{Ab1} was included in Eq. (3) to represent implicitly the effects of second-order $A\,^1\Sigma_u^+ - B\,^1\Pi_u - b\,^3\Pi_{1u}$ mixing.

B. Analytical representation of potential energy curves and spin-orbit functions

We chose to use an expanded Morse oscillator (EMO) model [29,30] to describe the potential curves of the interacting diabatic states $U_A(r)$ and $U_{b0}(r)$, as it is appropriate for the range of internuclear distances treated in the present analysis:

$$U_{A/b0}(r) = T_{\rm dis} - \mathfrak{D}_e + U_{\rm EMO}(r), \tag{4}$$

$$U_{\rm EMO}(r) = \mathfrak{D}_e[1 - e^{-\alpha(r)(r-r_e)}]^2$$
$$\alpha(r) = \sum_{i=0}^{N} a_i \left(\frac{r^p - r^p_{\rm ref}}{r^p + r^p_{\rm ref}}\right)^i, \tag{5}$$

where $T_{\rm dis}$ is the dissociation limit referenced to the minimum of the ground state, $\mathfrak{D}_e$ is the well depth, r_e is the equilibrium internuclear distance, parameter p is a fixed integer, and $r_{\rm ref}$ is chosen close to the minimum of the respective EMO function. The fixed energies of dissociation limits, $T^A_{\rm dis} = \mathfrak{D}^X_e + \Delta E_{\rm Rb} - \xi^{so}_{\rm Rb}$ and $T^{b0}_{\rm dis} = T^A_{\rm dis} - \xi^{so}_{\rm Rb}$, were calculated from the ground-state well depth, $\mathfrak{D}^X_e = 3993.53\ {\rm cm}^{-1}$ [31], the experimental spin-orbit parameter, $\xi^{so}_{\rm Rb} = [E_{5^2P_{3/2}} - E_{5^2P_{1/2}}]/3 = 79.198\ {\rm cm}^{-1}$ [32], and experimental $5^2P_{3/2} - 5^2S_{1/2}$ atomic transition energy, $\Delta E_{\rm Rb} = 12\,816.545\ {\rm cm}^{-1}$ [32].

The spin-orbit functions were also expressed analytically, using five-parameter Hulbert-Hirschfelder (HH) functions [33] to give more flexibility than the conventional three-parameter Morse form used in Ref. [11]:

$$\xi^{so}_{Ab0/A^{so}_{01}/A^{so}_{12}}(r) = \xi^{so}_{Rb} - \mathfrak{D}^{so}_e + U_{HH}(r), \tag{6}$$

$$U_{HH}(r) = \mathfrak{D}^{so}_e[(1-e^{-x})^2 + e^{-2x}x^3c(1+bx)]$$
$$x = a\left(r/r^{so}_e - 1\right), \tag{7}$$

where $\mathfrak{D}^{so}_e$ is the difference between the minimum of the spin-orbit function observed at the internuclear distance r^{so}_e and its limiting value. The initial parameters of the EMO and HH functions were extracted from quasirelativistic *ab initio* electronic structure calculations [11] using Le Roy's program BetaFit [34].

C. Computational details of fitting procedure

An analytical mapping procedure, based on a reduced variable representation of the radial coordinate, $y(r;\bar{r},\beta) =$

TABLE II. Spread of the experimental term values (in $\rm cm^{-1}$) available for the $A\,^1\Sigma_u^+ - b\,^3\Pi_u$ complex of Rb_2. PW- present work.

Source	E_{A-b}	J_{A-b}	Number of terms		
			$^{85}Rb_2$	$^{85}Rb\,^{87}Rb$	$^{87}Rb_2$
$A-b \rightarrow X$ LIF, LAC [10,20]	10816–14171	6–242	242	171	6
$A-b \rightarrow X$ LIF, Lyon [11]	10855–11396	17–157	207	183	4
$A-b \leftarrow X$ excitation, Temple [11]	11440–12316	14–107	456		
$(2)\,^1\Pi_g \rightarrow A-b$ LIF, LAC [5]	14100–16340	6–98	212	184	
$A-b \rightarrow X$ LIF, Riga, PW	10801–13030	8–258	834	464	43
$A-b \rightarrow X$ LIF, Lyon, PW	11644–13457	12–198	98	61	
$(2)\,^1\Pi_g \rightarrow A-b$ LIF, Lyon, PW	13990–16400	24–130	1342	1722	

$[1+(\bar{r}/r)^{\beta}]^{-1}$, was used to reduce the required number of mesh points and diminish the computational effort for the uniform finite-difference grid solution of the CC equations (1). The optimal mapping parameters, $\bar{r} = 5.5$ Å and $\beta = 4$, were determined by one-dimensional minimization of the overall discretization error. The system of four modified CC equations (1) given explicitly in Ref. [35] was solved in the interval $r \in [2.5, 15.0]$ Å by the boundary value method [36] using the central five-point finite-difference approximation of the kinetic-energy term. The ordinary eigenvalue and eigenfunction problem of the resulting symmetric band matrix was iteratively solved by the implicitly restarted Lanczos method realized in ARPACK software [37].

The parameters of the potential curves and spin-orbit functions were optimized iteratively using the nonlinear least-squares fitting (NLSF) procedure [25], minimizing the sum of squared deviations between the experimental data and model predictions,

$$\min\left\{\sum_{j=1}^{N_{\rm expt}} \frac{w_j\left(E_j^{\rm expt} - E_j^{CC} + \delta_j\right)^2}{N_{\rm expt} - n_p}\right\}, \tag{8}$$

where the weight of each datum w_j is expressed as a function of its experimental uncertainty σ_j, $w_j = 1/\sigma_j^2$; $E_j^{\rm expt}$ is the experimental term value; n_p is the total number of adjusted parameters of the model; and $N_{\rm expt}$ is the number of experimental term values involved in the fit. In the initial stages of the fitting process, it was useful to perform a robust weighting procedure to diminish an undesired effect of incorrectly assigned lines. In this case the weight of each experimental term value changes at each iteration depending on its deviation from the model prediction [38]:

$$w_j = \frac{1}{\sigma_j^2 + \left(E_j^{\rm expt} - E_j^{CC} + \delta_j\right)^2/3}. \tag{9}$$

The functional (8) was evaluated using the modified Levenberg-Marquardt algorithm [39] realized in MINPACK software [40].

Additional variables δ_j were included in Eq. (8) to compensate systematic (constant) shifts between term values obtained in Orsay, Philadelphia, Riga, and Lyon. These parameters, given in Table III, reveal significant discrepancies in the calibration of *a priori* very similar instruments. We have adopted wave numbers from OODR-excited LIF spectra as a reference, because they contain Rb 6*S*-5*P* and Rb 4*D*-5*P* atomic lines against which the FT spectra could be recalibrated if necessary.

Some constraints (based on *ab initio* calculations for the potential energy curves and spin-orbit functions [11]) were built into the minimization procedure to ensure physically reasonable extrapolation of the final semiempirical functions outside the region covered by the present experimental data set.

The experimental term values of the $^{85}Rb_2$ and $^{85}Rb\,^{87}Rb$ molecules were included in the fitting procedure stepwise, starting from the lowest vibrational levels of the $A\,^1\Sigma_u^+$ state and moving upwards to the $Rb(5\,^2S_{1/2}) + Rb(5\,^2P_{1/2})$ dissociation limit.

TABLE III. Empirically determined systematic shifts δ_j (cm^{-1}) applied to the $A-b$ term values established from $A-b \leftrightarrow X$ transitions recorded in different labs.

LAC [10,20]	Lyon [11]	Riga PW	Temple [11]
$A-b \rightarrow X$ LIF FT spectroscopy			$A-b \leftarrow X$ excitation polarization spectroscopy
0.021	–0.022	0.006	0.014

V. RESULTS AND DISCUSSION

A. Interatomic potentials and spin-orbit functions

The nonlinear least-squares fitting procedure (8) returned optimized parameters for the EMO potential energy curves (PECs) (Table IV), diagonal and off-diagonal state-of-charge functions defined by the Hulbert-Hirschfelder potential (Table V), and a set of four r-independent parameters δ_j compensating the systematic shifts of the experimental term values (Table III). These parameters reproduce in all ~6100 experimental term values with an unweighted standard deviation of 0.005 cm^{-1}, slightly smaller than the given experimental uncertainties ($\leqslant$0.01 cm^{-1}).

Table VI compares our work with earlier deperturbation analysis [11] and recent *ab initio* results [11,41,42]. The theoretical equilibrium parameters obtained recently in the

TABLE IV. EMO parameters for the diabatic potential energy curves of the deperturbed $A\,^1\Sigma_u^+$ and $b\,^3\Pi_{0u}$ states. $T_{\rm dis}$ and $\mathfrak{D}_e$ are in cm^{-1}, $r_{\rm ref}$ and r_e in Å, a_i in $Å^{-1}$, and p is dimensionless. Many digits are given for a_i to avoid rounding errors.

	$A\,^1\Sigma_u^+$	$b\,^3\Pi_{0u}$
	Fixed	
$T_{\rm dis}$	16731.197	16651.999
p	3	3
$r_{\rm ref}$	5.0	5.0
	Fitted	
$\mathfrak{D}_e$	5981.4463	7065.5350
r_e	4.87332	4.16071
a_0	0.459071419191528	0.583680705982008
a_1	0.0419509157494478	0.147739918699114
a_2	0.0221332536775103	0.0792242235679833
a_3	0.0882195817298351	0.128443062527828
a_4	–0.0427274943359167	–0.0542465192090390
a_5	0.0493532707713353	–0.223373559469424
a_6	0.4021772665842270	0.363456189186409
a_7	0.2190591463993592	–0.381863414606737
a_8	–1.776508778331850	–2.091277945277320
a_9	–1.51011277775665	–0.326913404154649
a_{10}	3.825616895554750	2.13193781881831
a_{11}	4.798499556916840	–0.193694483065469
a_{12}	–1.67576861912255	1.129287433283580
a_{13}	–10.8136153149462	7.2384052665076(-7)
a_{14}	–3.28143468932430	–0.822357644754994
a_{15}	7.051907640823940	5.02818163164330
a_{16}	0.204835695083045	–0.9189515320494410
a_{17}	6.052310439174940	–8.963735530614090
a_{18}	3.535251679582740	–0.498486329548209
a_{19}	–7.34901245700596	5.176882382471290

TABLE V. The empirical Hulbert-Hirschfelder parameters obtained for the diagonal, A^{so}_{01} and A^{so}_{12}, and off-diagonal ξ^{so}_{Ab0} spin-orbit functions. $\mathfrak{D}^{so}_e$ in cm^{-1}, r^{so}_e in Å, and a, b, and c are dimensionless. The dimensionless coupling parameter $\zeta^{so}_{Ab1} = 0.0270762$. Many digits are given to avoid rounding errors.

	ξ^{so}_{Ab0}	A^{so}_{01}	A^{so}_{12}
$\mathfrak{D}^{so}_e$	25.7777	14.1593	15.9406
r^{so}_e	5.31634	6.03760	5.60174
a	3.0787505945426	2.9786376722780	3.2318048464353
b	0.4451543837035	0.1743263228384	0.3174991047839
c	0.4587371400113	0.1078456292420	0.2058295712497

framework of pure Hund's "c" case coupling [42] are close to the present empirical values. At the same time, the present empirical electronic energy T_e and equilibrium distance r_e value obtained for the triplet $b\,^3\Pi_{0u}$ state are significantly different to those of the preceding analysis [11]. Figure 5 shows that we now have more information on levels with dominantly triplet character below 10 800 cm^{-1} than before, influencing the extrapolation back to the minimum of the $b\,^3\Pi_u$ potential. However, as we are still extrapolating over 1120 cm^{-1} back to the potential minimum, T_e is still best considered as reliable to $\sim$1 cm^{-1}, even though fitting statistics give a smaller uncertainty. The functions defined in this work have successfully overcome at least some of the problems detailed in the earlier analysis, where the authors highlighted unexplained large residuals at $J_{A-b} \sim 70$, $E_{A-b} = 11\,747$ cm^{-1}; these levels are now described by the fit.

Figure 6 compares the *ab initio* and empirical diagonal and off-diagonal spin-orbit functions. A scaling factor of $\sqrt{2}$ has been applied to the ξ^{so}_{Ab0} given by [11], since our diagonal spin-orbit matrix element $\sqrt{2}\xi^{so}_{Ab0}$ corresponds to the ξ^{so}_{Ab0} defined in Ref. [11]. The resulting PECs and spin-orbit (SO) functions are well defined in the range $r \in [2.8,\ 12.0]$ Å and they are available in pointwise form as Supplemental Material [22], which also lists a complete set of experimental and calculated rovibronic term values of the complex, together with (obs.–calc.) residuals and fractional partitions. Term energies and wave-function characteristics for arbitrary J_{A-b} levels can be also predicted for all isotopologs and are available upon request to A. Stolyarov.[1]

TABLE VI. Comparison of the empirical and *ab initio* electronic T_e energies (cm^{-1}) as well as equilibrium distance r_e (Å) of the $A\,^1\Sigma^+_u$ and $b\,^3\Pi_{0u}$ states. The symbol † denotes the *ab initio* data calculated without spin-orbit effects, corresponding to the $b^3\Pi_{1u}$ component.

	$A\,^1\Sigma^+_u$		$b\,^3\Pi_{0u}$	
Source	T_e	r_e	T_e	r_e
		Ab initio		
[11]	10915	4.90	9777†	4.19†
[41]	10853	4.87	9996†	4.16†
[42]	10747	4.87	9510	4.17
		Empirical		
[11]	10749.74	4.874	9601	4.132
This work	10749.75	4.873	9586.46	4.161

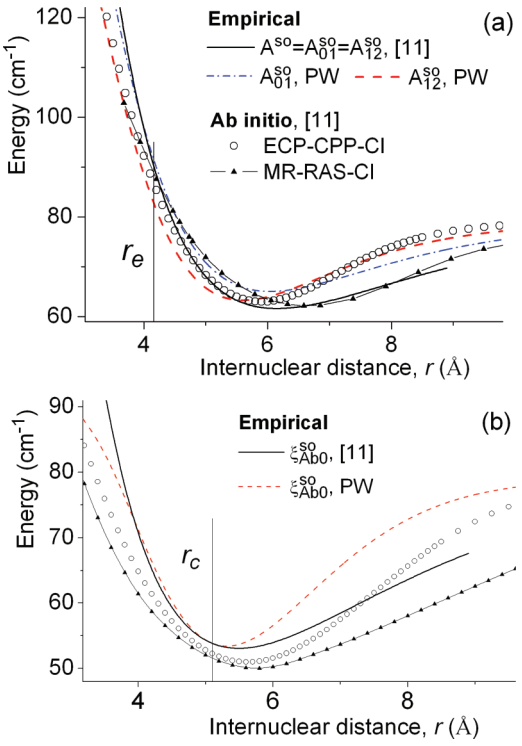

FIG. 6. (Color online) Comparison of empirical and *ab initio* spin-orbit functions. (a) Diagonal SO functions. r_e indicates the equilibrium distance for the $b\,^3\Pi_{0u}$ state. (b) Off-diagonal SO coupling function between the $A\,^1\Sigma^+_u$ and $b\,^3\Pi_{0u}$ states. r_c indicates internuclear distance at the crossing of diabatic PECs of interacting states.

The fraction partition analysis of the nonadiabatic vibrational wave functions (see Fig. 7) gives some physical insight into the nature of the present data. In this instance, it is clear that the $\Omega = 2$ component of the $A - b$ complex is still not well represented, and this suggests that the spin-orbit function A^{so}_{12} should be considered with caution; it will be much less reliable than A^{so}_{01}, derived from a well-balanced data set.

VI. SIMULATION OF ISOTOPIC SHIFT AND RELATIVE INTENSITY DISTRIBUTION

A. Term values for $^{87}Rb_2$

Optimization of energies obtained within the framework of an NLSF procedure typically leads to determination of local minimum of the functional (8) and, hence, it does not necessary give a unique solution. It is therefore useful to have some independent confirmation of the reliability of the deperturbation model. Isotopic energy-level shifts in the mixed $A - b$ rovibronic levels of Rb_2 can provide a rigorous test of the quality of both $A\,^1\Sigma^+_u$ and $b\,^3\Pi_{u0}$ PECs derived in course of the nonadiabatic analysis. Term values of the $^{87}Rb_2$ isotopolog were predicted using the mass-invariant fitting parameters obtained above from the simultaneous fit of $^{85}Rb_2$ and $^{85}Rb\,^{87}Rb$ energies, changing only the reduced mass

[1] avstol@gmail.com

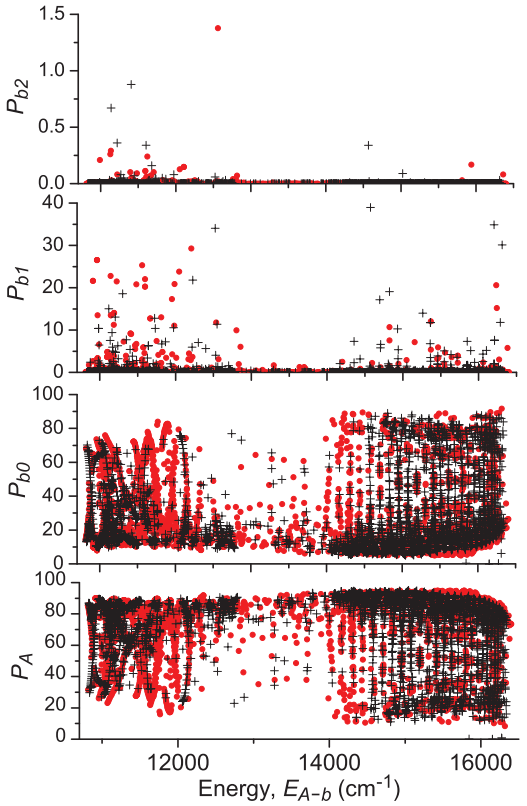

FIG. 7. (Color online) Partition of the nonadiabatic wave functions $P_i = \langle\phi_i|\phi_i\rangle$ (in %) of the $A - b$ complex as a function of term energy E_{A-b}. Black crosses represent observations for ^{85}Rb ^{87}Rb and circles (red online) ^{85}Rb$_2$ data points.

$\mu_{^{87}\mathrm{Rb}_2}$ in the CC equations (1)–(3). The calculated term values (see Table VII) coincide with their experimental counterparts within a standard deviation of 0.0045 cm^{-1}, which is close to the SD of the fit of ^{85}Rb$_2$ and ^{85}Rb^{87}Rb data.

B. Intensity distributions in the LIF progressions

Our spectra provide relative intensity information as well as line positions. We can use this to validate our results, by calculating wave functions from the potential curves and coupling matrix elements determined from energy-level fits, and compare with observations.

1. $(2)\,^1\Pi_g \rightarrow A\,^1\Sigma_u^+$ *fluorescence: Franck-Condon patterns*

We first considered the patterns seen in the OODR experiment, where experiment seemed to indicate that all useful results came from an energy window <300 cm^{-1} wide, coming from upper-state levels with $v' > 35$. According to the *ab initio* calculations [42], the transition dipole moment for the $(2)\,^1\Pi_g - A\,^1\Sigma_u^+$ system is almost invariant with internuclear distance, so this should be a Franck-Condon effect. Using the adiabatic PEC for the A state given in supplementary data, and an approximate potential curve for the $(2)\,^1\Pi_g$ state (calculated with the data given by Han *et al.* [24] plus fragmentary information from the levels observed in this work), we explain this energy window with Franck-Condon intensity patterns. Filtering out the very strong $A \rightarrow X$ fluorescence sacrifices a

TABLE VII. The experimental rovibronic term values E^{expt}_{A-b} (in cm^{-1}) of the $A\,^1\Sigma_u^+ - b\,^3\Pi_u$ complex assigned to ^{87}Rb$_2$ isotopolog. $O - C = E^{\mathrm{expt}} - E^{CC}$ (in cm^{-1}) is the difference between experimental and predicted energies. $P_i = \langle\phi_i|\phi_i\rangle$ (in %) are the fraction partitions of the levels.

J_{A-b}	E^{expt}_{A-b}	$O - C$	P_A	P_{b0}	P_{b1}
		Riga, PW			
59	10851.139	0.000	86.7	13.3	0.0
64	10861.646	0.001	85.3	14.7	0.0
66	10866.099	–0.001	84.5	15.5	0.0
68	10870.700	0.001	83.5	16.5	0.0
69	10873.051	–0.005	83.0	17.0	0.0
70	10875.450	0.001	82.4	17.6	0.0
72	10880.354	–0.000	81.0	19.0	0.0
74	10885.419	0.001	79.2	20.7	0.0
76	10890.653	0.005	77.1	22.8	0.0
81	10904.514	0.003	69.7	30.3	0.0
86	10919.636	–0.001	59.3	40.6	0.1
89	10929.380	0.004	52.9	47.1	0.1
82	11015.683	–0.003	87.4	11.7	0.9
85	11024.103	0.002	87.6	12.1	0.3
130	11074.453	–0.001	76.1	17.5	6.3
145	11146.850	–0.000	53.0	46.9	0.1
109	11173.538	0.005	68.4	31.6	0.0
77	11180.151	0.003	51.4	48.5	0.0
144	11193.661	0.001	89.4	10.5	0.1
158	11205.589	0.008	84.1	15.8	0.1
180	11329.241	0.003	75.8	24.1	0.1
172	11338.243	0.006	85.4	12.3	2.3
125	11340.886	0.005	53.7	46.1	0.1
174	11349.622	0.002	86.2	13.0	0.8
176	11361.127	0.004	85.8	13.8	0.4
178	11372.773	0.005	85.1	14.7	0.3
180	11384.574	0.006	84.0	15.8	0.2
182	11396.540	0.004	82.6	17.3	0.2
184	11408.692	0.006	80.7	19.2	0.2
148	11456.910	0.001	55.9	43.9	0.2
20	12113.034	-0.009	86.8	13.2	0.0
22	12114.399	-0.007	87.0	13.0	0.0
24	12115.886	-0.010	87.2	12.8	0.0
26	12117.502	-0.008	87.5	12.5	0.0
28	12119.241	-0.008	87.7	12.3	0.0
30	12121.108	-0.005	88.0	12.0	0.0
32	12123.101	-0.002	88.2	11.8	0.0
75	12234.881	-0.002	81.8	16.4	1.8
77	12239.778	0.003	83.9	15.8	0.4
79	12244.777	0.005	84.7	15.2	0.2
81	12249.891	0.006	85.1	14.8	0.1
83	12255.117	0.002	85.3	14.6	0.1
130	12331.059	-0.002	44.4	55.4	0.1
		LAC [10,20]			
45	10826.334	0.007	88.6	11.4	0.0
157	11200.319	0.001	83.8	16.2	0.1
72	12150.848	0.004	74.7	25.3	0.0
52	13348.276	0.004	87.0	13.0	0.0
78	13499.610	-0.007	87.0	13.0	0.0
82	13646.144	-0.002	87.1	12.9	0.0

good deal of information on the $A-b$ complex. [Our attempts to pursue $(2)\,^1\Pi_g \rightarrow A-b$ fluorescence series into the tail of the $A \rightarrow X$ fluorescence by reducing optical filtering failed. So did attempts to record "difference" spectra (possible with two color experiments, pumping the intermediate level via $P(J+1)$ then $R(J-1)$, for example, and examining the features common to both), because so many transitions were excited alongside the one of interest.]

2. $A\,^1\Sigma_u^+ - b\,^3\Pi_u \rightarrow X\,^1\Sigma_g^+$ *fluorescence*

More stringent tests were imposed by calculating intensity distributions for the $A-b \rightarrow X$ series, coming from the strongly mixed $A-b$ levels, as a nodal structure of nonadiabatic vibrational wave functions [43] provide a sensitive independent test of the quality of energy-based deperturbation analysis performed above. In the present study, the relative intensities of $A-b \rightarrow X$ rovibronic transitions were estimated in accordance with the relation

$$I - \nu_{A-b\rightarrow X}^4 M^2, \tag{10}$$

in which $\nu_{A-b\rightarrow X}$ is the transition wave number and transition probability $M_{(A-b)-X}$ is defined as

$$M = \langle \phi_A | d_{A-X} | v_X'' \rangle, \tag{11}$$

where ϕ_A represents the fraction of the $A\,^1\Sigma_u^+$ state in the total nonadiabatic wave function Ψ^{CC} of the $A-b$ complex. $|v_X''\rangle$ is the adiabatic vibrational wave function of the ground $X\,^1\Sigma_g^+$ state obtained by solution of a single-channel radial Schrödinger equation with the accurate empirical potential given in Ref. [10]. Since the $b\,^3\Pi_u \rightarrow X\,^1\Sigma_g^+$ transitions are formally spin-forbidden in the present pure Hund's case "**a**" coupling, the contribution to the $A-b \rightarrow X$ transition probability $M_{(A-b)-X}$ comes only from the spin-allowed $A\,^1\Sigma_u^+ \rightarrow X\,^1\Sigma_g^+$ transition. The required *ab initio* transition dipole moment function d_{A-X} is available in Refs. [42] and [44].

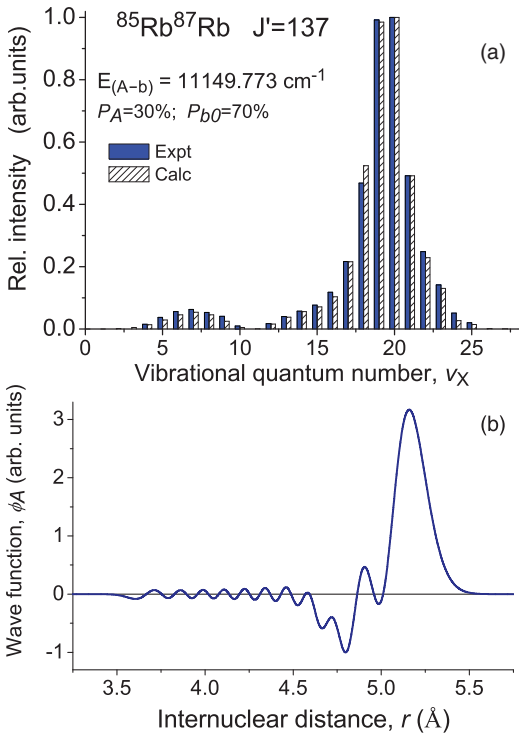

FIG. 8. (Color online) (a) The experimental and predicted relative intensity distributions of $A\,^1\Sigma_u^+ - b\,^3\Pi_u(J=137) \rightarrow X^1\Sigma_g^+(v_X'')$ transitions. (b) The corresponding nonadiabatic wave function of the (nominally singlet, $A\,^1\Sigma_u^+$) upper state. P_A and P_{b0} are the fractions of the singlet and triplet state, respectively. The adiabatic vibrational quantum numbers are $v_A = 0$ and $v_{b0} = 22$.

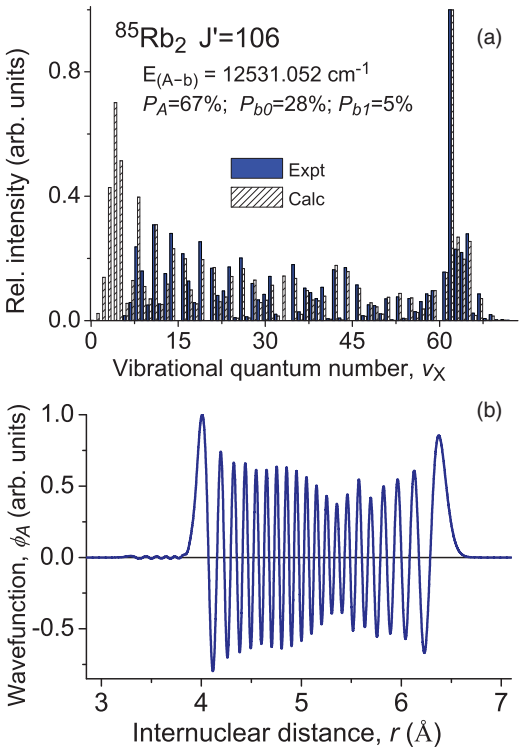

FIG. 9. (Color online) (a) The experimental and predicted relative intensity distribution of $A\,^1\Sigma_u^+ - b\,^3\Pi_u(J=106) \rightarrow X^1\Sigma_g^+(v_X'')$ transitions. (b) The corresponding nonadiabatic wave function of the (nominally singlet, $A\,^1\Sigma_u^+$) upper state. Transitions to $v_X'' = 0$–5 levels were suppressed by an optical filter in the experiments. P_A, P_{b0}, and P_{b1} are the fractions of the singlet and triplet states, respectively. Adiabatic vibrational quantum numbers are $v_A = 39$ and $v_{b0} = 52$.

Relative intensity distributions were simulated for several $A-b \rightarrow X(v'')$ fluorescence series and compared with their experimental counterparts, corrected for instrumental response [45]. Intensities obtained for P and R branches were averaged both for observation and calculation. In most cases (see, for example, Figs. 8 and 9), the predicted intensity distributions match their experimental counterparts within the experimental uncertainty estimated as 15%. Figure 8 illustrates breakdown of the conventional one-dimensional oscillation theorem [46] taking place for strongly coupled A and b states, since the number of nodes of the nonadiabatic vibrational eigenfunction $\phi_A(r)$ differs from its adiabatic counterpart, in this case $v_A = 0$. The second (unexpected) maximum in the intensities allowing $v_X'' = 3-10$ to be observed arises from the contribution of $v_b = 22$. This effect is generally less obvious at first glance in the higher levels of the singlet A state (see Fig. 9), where the nodal structure is less affected by local perturbations. However, it often leads to an interference (non Franck-Condon patterns) structure of the relevant LIF spectra, especially for transitions to high vibrational levels v_X'' of the ground X state.

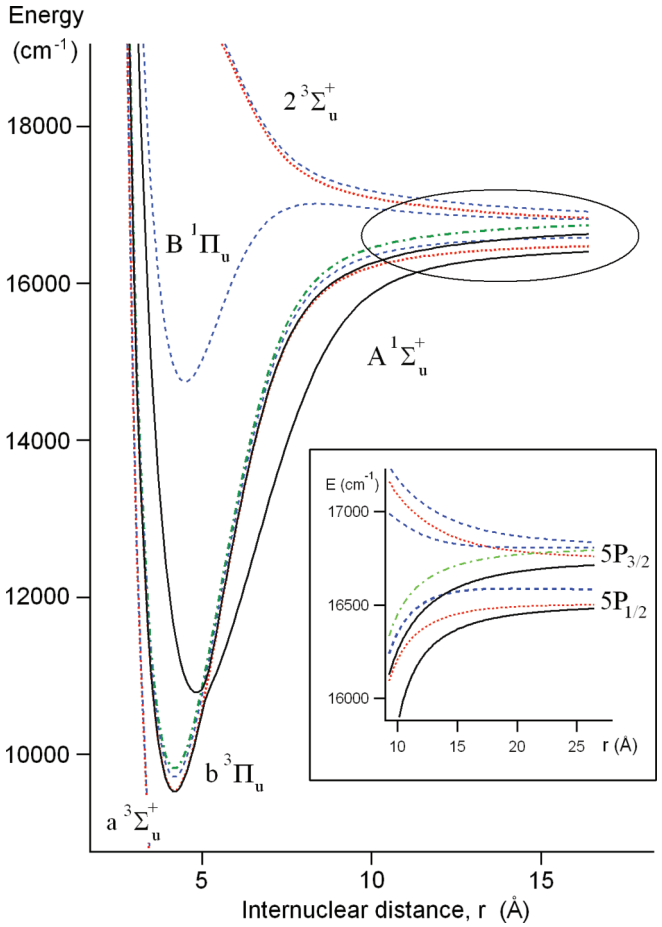

FIG. 10. (Color online) $\Omega = 0$, 1, and 2 components of *ungerade* electronic states dissociating to Rb($5s$) + Rb($5p$) atoms, indicating case "a" parentage, taken from Ref. [42]. The inset enlarges the region where our model breaks down, as the 1_u and 0_u^+ components from the parent $b\,^3\Pi_u$ state cross before converging to their respective atomic products. Key: (red) dots 0_u^-, (black) solid line 0_u^+, (blue) dashes 1_u, (green) dot-dash 2_u.

VII. CONCLUSIONS

This work has extended the analysis of the $A - b$ complex in Rb_2 begun by Salami *et al.* [11], as the model now reproduces observed term energies between 14 000 and 16 400 cm^{-1}. The $A\,^1\Sigma_u^+$ and $b\,^3\Pi_{0u}$ states remain very heavily mixed throughout this region. In terms of the pure Hund's "**a**" case coupling, this represents an extension from $v_A \sim 85$ in the earlier work to $v_A \sim 185$ now, with outer turning points around 11.7 Å. Including information on some term values of the $A - b$ complex below 10 800 cm^{-1} with dominantly triplet character, and taking appropriate steps to compensate systematic shifts due to calibration issues in the spectra, we have improved the rms residual of the fit achieved in [11] by a factor of about 10. Thus we have now achieved a full description of the 0_u^+ levels in the short-range part of the $A - b$ complex and can use this to predict optimum wave function mixing at low J values for triplet-singlet transfer in cold molecular samples with confidence, for all three isotopologs. The relative accuracy of the predicted term values is estimated to be about 0.005 cm^{-1}, even if their absolute uncertainties may be 3–4 times larger (because of our choice of reference energies and shifts applied to data sets).

We have used energy-level predictions for $^{87}Rb_2$ as well as intensity patterns in the $A - b \rightarrow X$ systems to validate our model, assuming the single-spin-allowed $A - X$ transition dipole moment contribution. The wave-function character plots show that our data set describes the 0_u^+ components of these electronic states rather well, except for the lowest "dark" vibrational levels of the $b\,^3\Pi_{0u}$ state lying below the minimum of the singlet A state. We still have no information on dominantly $b\,^3\Pi_{1u}$ levels, but have enough data to describe the diagonal spin-orbit function A_{01}^{so} over a range of internuclear distance 2.9–9.6 Å. The extensions are of course influenced by the functional form we chose to impose. Introducing the second spin-orbit function A_{12}^{so} has certainly improved the standard deviation of the fit, allowing more flexibility than the earlier analysis [11], but this function is less reliable because it is influenced by a much smaller fraction of the existing data set. Future work on this project will need to focus on experimental routes directly to the higher components, looking at fluorescence from higher-lying $^3\Lambda_g$ states (as for NaK [47] or K_2 [8], for example), to pin down the lowest energy levels of the $b\,^3\Pi_u$ state and to tighten the definition of the spin-orbit functions.

A more sophisticated representation of the potential energy curves [48,49] will be required to extend this work into the region where van der Waals forces dominate, approaching the $5\,^2S_{1/2} + 5\,^2P_{1/2;3/2}$ asymptotes more closely. Current observations still stop about 200 cm^{-1} below the lowest 0_u^+ levels seen in cold-atom association [50]. Our analytical function approach requires more data for the higher vibrational levels in order to define the flatter parts of the diagonal and off-diagonal spin-orbit functions (see Fig. 6) beyond 10 Å. Direct observation of levels with $b\,^3\Pi_u$ character would obviously be most helpful here. As indicated in Ref. [50], and illustrated in Fig. 10, the levels closer to the $^2P_{3/2}$ asymptote will be progressively less well described by this model as interactions with higher-lying $B\,^1\Pi_u$ and $(2)^3\Sigma_u^+$ states also come into play. At this stage, the "four-coupled-channels" picture is no longer adequate.

ACKNOWLEDGMENTS

We are very grateful to O. Dulieu and C. Amiot for making available some archived spectra of Rb_2 from Laboratoire Aimé Cotton. The Riga group would like to thank A. Brasovs for help with the data processing, and gratefully acknowledges financial support from ERAF Grant No. 2010/0242/2DP/2.1.1.1.0/10/APIA/VIAA/036.

[1] X. B. Xie and R. W. Field, J. Mol. Spectrosc. **117**, 228 (1986).
[2] L. Li, Q. S. Zhu, A. M. Lyyra, T. J. Whang, W. C. Stwalley, R. W. Field, and M. H. Alexander, J. Chem. Phys. **97**, 8835 (1992).
[3] M. Tomza, M. H. Goerz, M. Musial, R. Moszynski, and C. P. Koch, Phys. Rev. A **86**, 043424 (2012).
[4] W. C. Stwalley, M. Bellos, R. Carollo, J. Banerjee, and M. Bermudez, Mol. Phys. **110**, 1739 (2012).

[5] C. Amiot, O. Dulieu, and J. Vergès, Phys. Rev. Lett. **83**, 2316 (1999).

[6] A. J. Ross, P. Crozet, C. Effantin, J. d'Incan, and R. F. Barrow, J. Phys. B **20**, 6225 (1987).

[7] M. Tamanis, R. Ferber, A. Zaitsevskii, E. A. Pazyuk, A. V. Stolyarov, H. Chen, J. Qi, H. Wang, and W. C. Stwalley, J. Chem. Phys. **117**, 7980 (2002).

[8] M. R. Manaa, A. J. Ross, F. Martin, P. Crozet, A. M. Lyyra, L. Li, C. Amiot, and T. Bergeman, J. Chem. Phys. **117**, 11208 (2002).

[9] T. Bergeman, C. E. Fellows, R. F. Gutterres, and C. Amiot, Phys. Rev. A **67**, 050501(R) (2003).

[10] J. Y. Seto, R. J. Le Roy, J. Vergès, and C. Amiot, J. Chem. Phys. **113**, 3067 (2000).

[11] H. Salami, T. Bergeman, B. Beser, J. Bai, E. H. Ahmed, S. Kotochigova, A. M. Lyyra, J. Huennekens, C. Lisdat, A. V. Stolyarov, O. Dulieu, P. Crozet, and A. J. Ross, Phys. Rev. A **80**, 022515 (2009).

[12] J. Bai, E. H. Ahmed, B. Beser, Y. Guan, S. Kotochigova, A. M. Lyyra, S. Ashman, C. M. Wolfe, J. Huennekens, F. Xie, D. Li, L. Li, M. Tamanis, R. Ferber, A. Drozdova, E. Pazyuk, A. V. Stolyarov, J. G. Danzl, H. C. Nagerl, N. Bouloufa, O. Dulieu, C. Amiot, H. Salami, and T. Bergeman, Phys. Rev. A **83**, 032514 (2011).

[13] O. Docenko, M. Tamanis, R. Ferber, E. A. Pazyuk, A. Zaitsevskii, A. V. Stolyarov, A. Pashov, H. Knockel, and E. Tiemann, Phys. Rev. A **75**, 042503 (2007).

[14] O. Docenko, M. Tamanis, R. Ferber, T. Bergeman, S. Kotochigova, A. V. Stolyarov, A. de Faria Nogueira, and C. E. Fellows, Phys. Rev. A **81**, 042511 (2010).

[15] J. Zaharova, M. Tamanis, R. Ferber, A. N. Drozdova, E. A. Pazyuk, and A. V. Stolyarov, Phys. Rev. A **79**, 012508 (2009).

[16] A. Kruzins, I. Klincare, O. Nikolayeva, M. Tamanis, R. Ferber, E. A. Pazyuk, and A. V. Stolyarov, Phys. Rev. A **81**, 042509 (2010).

[17] M. Tamanis, I. Klincare, A. Kruzins, O. Nikolayeva, R. Ferber, E. A. Pazyuk, and A. V. Stolyarov, Phys. Rev. A **82**, 032506 (2010).

[18] C. Amiot, P. Crozet, and J. Vergès, Chem. Phys. Lett. **121**, 390 (1985).

[19] B. Beser, V. B. Sovkov, J. Bai, E. Ahmed, C. C. Tsai, F. Xie, L. Li, V. S. Ivanoc, and A. M. Lyyra, J. Chem. Phys. **131**, 094504 (2009).

[20] C. Amiot, J. Chem. Phys. **93**, 8591 (1990).

[21] W. M. Gelbart and K. F. Freed, Chem. Phys. Lett. **18**, 470 (1973).

[22] See Supplemental Material at http://link.aps.org/supplemental/10.1103/PhysRevA.88.022504 for wave numbers of transitions recorded in this work, output from the least-squares fitting routines, and pointwise functions for potential energy curves and spin-orbit functions.

[23] C. Amiot and J. Vergès, Chem. Phys. Lett. **274**, 91 (1997).

[24] X. Han, X. Wang, T. Wang, W. Xiong, and X. Dai, Chem. Phys. Lett. **538**, 1 (2012).

[25] H. Lefebvre-Brion and R. W. Field, *The Spectra and Dynamics of Diatomic Molecules* (Academic Press, New York, 2004).

[26] P. Qi, J. Bai, E. Ahmed, A. M. Lyyra, S. Kotochigova, A. J. Ross, C. Effantin, P. Zalicki, J. Vigue, G. Chawla, R. W. Field, T. J. Whang, W. C. Stwalley, H. Knockel, E. Tiemann, J. Shang, L. Li, and T. Bergeman, J. Chem. Phys. **127**, 044301 (2007).

[27] C. Lisdat, O. Dulieu, H. Knockel, and E. Tiemann, Eur. Phys. J. D **17**, 319 (2001).

[28] H. Katô, Bull. Chem. Soc. Jpn. **66**, 3203 (1993).

[29] E. G. Lee, J. Y. Seto, T. Hirao, P. F. Bernath, and R. J. Le Roy, J. Mol. Spectrosc. **194**, 197 (1999).

[30] R. J. Le Roy, Y. Huang, and C. Jary, J. Chem. Phys. **125**, 164310 (2006).

[31] C. C. Tsai, R. S. Freeland, J. M. Vogels, H. M. J. M. Boesten, B. J. Verhaar, and D. J. Heinzen, Phys. Rev. Lett. **79**, 1245 (1997).

[32] J. Sansonetti, Phys. Chem. Ref. Data **35**, 301 (2006).

[33] H. M. Hulburt and J. O. Hirschfelder, J. Chem. Phys. **9**, 61 (1941).

[34] R. J. Le Roy, BetaFit, A computer program to fit pointwise potentials to selected analytic functions, http://leroy.uwaterloo.ca/programs, University of Waterloo Chemical Physics Research Report CP-666 (2013).

[35] V. V. Meshkov, A. V. Stolyarov, and R. J. Le Roy, Phys. Rev. A **78**, 052510 (2008).

[36] D. G. Truhlar, J. Comp. Phys. **10**, 123 (1972).

[37] R. B. Lenoucq, D. C. Sorensen, and C. Yang, ARPACK *Users' Guide: Solution of Large Scale Eigenvalue Problems with Implicitly Restarted Arnoldi Methods* (SIAM, Philadelphia, PA, 1997), p. 140.

[38] J. K. G. Watson, J. Mol. Spectrosc. **219**, 326 (2003).

[39] W. H. Press, S. A. Teukolsky, W. T. Vetterling, and B. P. Flannery, *Numerical Recipes in Fortran 77* (Cambridge University Press, Cambridge, UK, 1999).

[40] J. More, B. Garbow, and K. Hillstrom, MINPACK software for solving nonlinear equations and nonlinear least-squares problems, http://www.netlib.org/minpack, University of Chicago, Argonne National Laboratory (1999).

[41] J. Lozeille, A. Fioretti, C. Gabbanini, Y. Huang, H. K. Pechkis, D. Wang, P. L. Gould, E. E. Eyler, W. C. Stwalley, M. Aymar, and O. Dulieu, Eur. Phys. J. D **39**, 261 (2006).

[42] A. R. Allouche and M. Aubert-Frécon, J. Chem. Phys. **136**, 114302 (2012).

[43] V. I. Pupyshev, E. A. Pazyuk, A. V. Stolyarov, M. Tamanis, and R. Ferber, Phys. Chem. Chem. Phys. **12**, 4809 (2010).

[44] R. Beuc, M. Movre, V. Horvatic, C. Vadla, O. Dulieu, and M. Aymar, Phys. Rev. A **75**, 032512 (2007).

[45] The spectral sensitivity $S(\nu) = I^{\mathrm{Corr}}/I^{\mathrm{expt}} = 16.72 + 0.00038\nu - 19.0/(1 + e^{0.00324(\nu - 11350)})$ of the Fourier transform spectrometer of the Riga group operated with an InGaAs diode detector was determined in the near-infrared region $\nu \in [8250, 11\,700]$ cm^{-1} by a comparison of the semiempirical calculated KCs $A\,^1\Sigma^+ \rightarrow X\,^1\Sigma^+$ rovibronic transition probabilities with experimental relative intensity distribution in the relevant $A \rightarrow X$ LIF spectra.

[46] L. D. Landau and E. M. Lifshitz, *Quantum Mechanics* (Pergamon, New York, 1965).

[47] A. J. Ross, C. Effantin, J. d'Incan, and R. F. Barrow, J. Phys. B **19**, 1449 (1987).

[48] N. Dattani and R. J. Le Roy, J. Mol. Spectrosc. **267**, 199 (2011).

[49] R. J. Le Roy, C. C. Haugen, J. Tao, and H. Li, Mol. Phys. **109**, 435 (2011).

[50] T. Bergeman, J. Qi, D. Wang, Y. Huang, H. K. Pechkis, E. E. Eyler, P. L. Gould, W. C. Stwalley, R. A. Cline, J. D. Miller, and D. J. Heinzen, J. Phys. B **39**, 813 (2006).